Journal of Energy Storage 54 (2022) 105306

Contents lists available at ScienceDirect

Journal of Energy Storage

journal homepage: www.elsevier.com/locate/est

Research Papers

Electro-thermal modelling of redox flow-batteries with electrolyte swapping for an electric ferry

Richard Woodfield [a,*], Stephen Glover [a], Robert Watson [b], Peter Nockemann [c], Richard Stocker [d]

[a] School of Mechanical and Aerospace Engineering, Queen's University Belfast, Belfast BT7 1NN, Northern Ireland, United Kingdom of Great Britain and Northern Ireland
[b] School of Aeronautical and Automotive Engineering, Loughborough University, Loughborough, LE11 3TU, England, United Kingdom of Great Britain and Northern Ireland
[c] School of Chemistry, The QUILL Research Centre, Queen's University Belfast, Belfast BT9 5AG, Northern Ireland, United Kingdom of Great Britain and Northern Ireland
[d] Horizon Scanning, HORIBA MIRA, Nuneaton CV10 0TU, England, United Kingdom of Great Britain and Northern Ireland

ARTICLE INFO

Keywords:
Vanadium redox flow battery
Electrical equivalent circuit modelling
Maritime
Electric ferry
Decarbonisation

ABSTRACT

Vanadium redox flow-batteries in coastal ferry applications have the potential to help bring down the carbon footprint of the shipping industry. There is a lack of research focused on vanadium redox flow-batteries in transport applications due to their low energy density, though electrolyte swapping offers benefits whereby the depleted electrolyte can be rapidly exchanged for a fully charged supply. Vanadium redox flow-batteries also benefit from significantly higher cycle life when compared to Li-ion and fuel cell technologies, offering potential for lower cost per year of ownership. A vanadium redox flow-battery coastal ferry is electro-thermally modelled to identify whether it is feasible in terms of energy capacity, temperature limits, carbon footprint and cost. The ferry journeys between two ports, where each port is equipped with a flow-battery to provide electrolyte swapping. An Equivalent Circuit Model is utilized to model the battery response, while the thermal model predicts the electrolyte temperature based on the conservation of energy. Shunt current and pumping losses are considered in the model. It was found that vanadium redox flow-batteries show real potential for the decarbonisation of the shipping industry. Battery temperature is kept within the safe operating limits, while offering a cost per voyage close to that of a diesel system, with significant reductions in CO_2 output.

1. Introduction

Ever increasingly stringent emissions regulations imposed by the International Marine Organization and the rising cost of oil prices are both major driving forces in the shift of the maritime industry towards greener power systems. Shipping accounts for 90 % of the transportation sector [1] and is responsible for 2.7 % of anthropogenic global CO_2 emissions [2]. In order to transition towards the imposed limits, the marine industry is using a number of approaches such as low emissions fuels [3], dual fuel [4] and LNG [5]. Additionally, there has been a rise in interest concerning ferry hybridization and *E*-Ferries, which are commonly powered by Li-ion [6], fuel-cells [7], hybrid fuel-cell-battery [8,9], or diesel hybrids.

Flow-batteries offer an alternative energy storage solution and are receiving growing interest in grid storage [10] and home storage applications [11,12]. Fig. 1 shows the general principle of vanadium redox flow-battery operation. The liquid electrolyte for each half-cell is pumped through a cell containing electrodes and a membrane, and Eqs. (1) and (2) describe the electrochemical half-cell reactions for an all-vanadium type flow-cell during charge and discharge respectively. The cells can be easily stacked resulting in a series electrical connection, while using a parallel manifold to feed the electrolyte.

$$V^{3+} + e^- \leftrightarrow V^{2+} \tag{1}$$

$$VO^{2+} + H_2O \leftrightarrow VO_2^+ + 2H^+ + e^- \tag{2}$$

Flow batteries have a number of benefits, such as easier control due to fast response times [13,14] when compared to Li-ion, a decoupled power-energy relationship allowing for precise system sizing, and a lifespan of 20 years [12]. No studies to date have explored the potential influence that vehicle vibrations or loading could have on this lifespan. The main limitations of a flow-battery are the low energy density of the electrolyte and the added system complexity due to the electrolyte network and associated pumps. The low energy density is less of an issue for stationary applications, where it is relatively easy to continue to

* Corresponding author.
E-mail address: rwoodfield01@qub.ac.uk (R. Woodfield).

https://doi.org/10.1016/j.est.2022.105306
Received 24 March 2022; Received in revised form 27 June 2022; Accepted 11 July 2022
Available online 18 July 2022

Nomenclature

T_{batt}	Temperature of the electrolyte in the battery (K)
T_+	Temperature of the electrolyte in the positive tank (K)
T_-	Temperature of the electrolyte in the negative tank (K)
T_{air}	Temperature of the surrounding air (K)
T_{port}	Temperature of the electrolyte in a port electrolyte tank (K)
C_p	Electrolyte specific heat (J kg^{-1} K^{-1})
ρ	Electrolyte density (kg m^{-3})
Ɛ	Electrode porosity
M_{batt}	Mass of the battery (kg)
V_{batt}	Volume of electrolyte inside the battery unit (m^3)
V_+	Volume of electrolyte inside the positive tank (m^3)
V_-	Volume of electrolyte inside the negative tank (m^3)
Q_+	Overall positive system flow rate (m^3 s^{-1})
Q_-	Overall negative system flow rate (m^3 s^{-1})
Q_{port}	Electrolyte exchange rate with a port (m^3 s^{-1})
U	Overall heat transfer coefficient of each tank (W m^{-2} K^{-1})
A	Overall surface area of each tank (m^2)
I_{stack}	Current of a single stack in the battery system (A)
R_{stack}	Resistance of a single stack in the battery system (Ω)
n_{string}	Number of stacks in the battery system
n_{stack}	Number of cells per stack in the ferry
SoC	State of charge (%)
R_{gc}	Stack guide channel resistance (Ω)
$R_{manifold}$	Stack manifold resistance (Ω)
$R_{connector}$	Stack manifold to string connector resistance (Ω)
$R_{strmanifold}$	Manifold section between each stack resistance (Ω)
p	Pressure (Pa)
t_{port}	Time spent at a port (s)

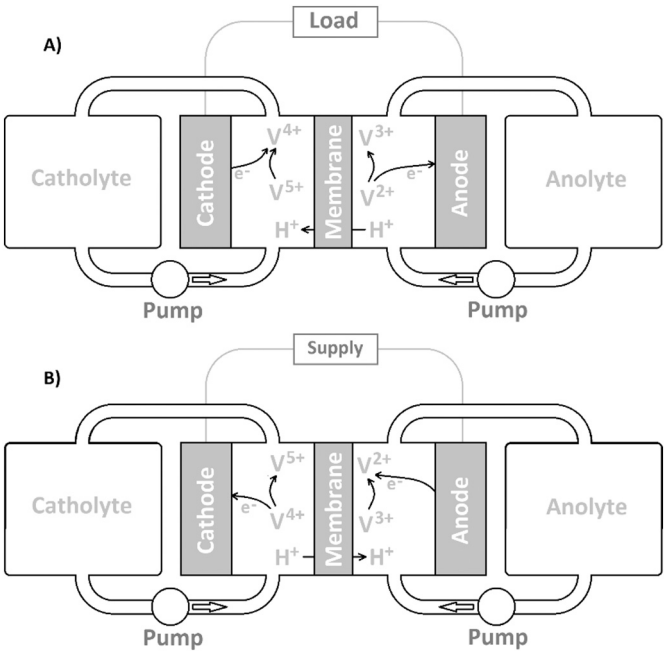

Fig. 1. A Vanadium Redox Flow-Battery reaction during discharge (a), and charge (b).

expand the size of the storage tanks over time if required [15]. For transport applications, where vehicle mass and space is severely restricted, electrolyte swapping presents an opportunity for the use of this technology. Since the charge is stored within the liquid electrolyte, the discharged electrolyte can be swapped rapidly for a fresh charge, in addition to being capable of regular recharging methods.

Redox flow-batteries have received very limited research in transport applications, which could be attributed to the aforementioned low energy density. Mohamed et al. first modelled the use of a vanadium redox flow-battery series hybrid vehicle by means of scaling results from a lab-scale flow-battery experiment [16]. It was concluded that the flow-battery was comparable to lead-acid with the added benefit of electrolyte swapping. However, the energy efficiency value obtained and used in the model was just 65 %, compared to the expected value of between 80 and 90 % [17]. Campillo et al. later modelled the use of a vanadium redox flow-battery in a wheel-loader, which is a heavy off-road vehicle application [18]. It was found that the application was feasible, though impractical due to the required frequency of recharging. More recently, Barelli et al. modelled a vanadium redox flow-battery and Li-ion hybrid bus, and compared it to that of a pure Li-ion, and a fuel-cell Li-ion hybrid [19]. The flow-battery covered the nominal load while the Li-ion handled the dynamic peaks. The model considered that each bus configuration would attempt to complete as many journeys as possible in a 12-hour timeframe. The flow-battery hybrid simulation showed real potential, with longer net driving time and a greater system lifespan than the other two configurations [19].

With such a low energy density it is clear that, for transport applications, the vanadium redox-flow battery would be best suited to a vehicle that has sufficient space to house the excessive volume of electrolyte required. This paper shifts the attention towards the use of flow-batteries in coastal ferry applications. Recently, two projects have emerged showing an interest in the application of RFB technology in the maritime sector, though no publications exist to date. FLO-MAR investigated the use of RFB system in various vessel types and found that the technology was best suited to short range vessels, such as wind farm support, ferries, port and harbour vessels, and leisure crafts [20]. BlueStor recently concluded in an initial feasibility study that a 50 MW/600MWh installation on a cruise ship would be more compact than a Lithium-ion system, and plan to continue their work into the prototype phase [21]. Table 1 highlights percentages of the global fleet with respect to the size of the vessel, where the ferry modelled in this paper falls in the medium category.

When modelling a battery in any particular application, it is necessary to understand the battery dynamic response to an applied load. The main reasons for this is to determine if the system remains within the safe voltage/power limits throughout the cycle and to evaluate the heat generated due to overpotential response with time. This can be achieved using first-principle models [23] which are then validated by test data, though an alternative is to use electrical equivalent circuit models (ECMs), which are data driven. First principle models often require a lot of information about the battery, which the control system designer may not have access to, though typically provide a higher degree of accuracy when all of the relevant information is present. ECMs utilize the behavior of electrical components to mimic the battery response and are computationally light-weight and still yield good accuracy, making

Table 1
Different vessel types as a percentage of the global fleet [22].

Vessel	Vessel size (gross tonnage)	% of Global Fleet	
		By total number	By gross tonnage
Small	<500	37	1
Medium	500–25,000	43	17
Large	25,000–60,000	13	34
Very large	>60,000	7	48

them ideal of on-board battery management systems. A number of flow-battery ECM models have been developed [24–26], and it has been found that a single-order ECM is sufficient to accurately model flow-battery behavior [24], which will be adopted in this study.

Another important aspect when assessing the feasibility of an energy storage system is whether the temperature will exceed the safe-operating conditions. Vanadium redox flow-batteries should ideally be kept operating between 5 °C to 40 °C. If the lower or upper threshold is crossed, precipitation of V^{2+}/V^{3+} and V^{5+} occurs respectively [27]. A number of temperature models have been developed thus far for flow-batteries [27–29], where the current paper will be modelling electrolyte temperature using energy balance equations.

The cost associated with battery production and degradation is also an important aspect when exploring feasibility. There has been little research into the cost of flow-battery manufacture, though since the power and energy relationship is decoupled, the costs associated are too. Power costs are defined as anything related to the battery stack, including battery components, pumps, assembling, testing, and power management. Energy costs are then mostly related to the electrolyte and tanks. The power and energy costs are approximately 1980 $/kW and 227 $/kWh respectively [30], though this can be expected to drop dramatically if production was scaled up and if the technology received more research attention. Finally, the global warming potential (GWP) will be considered, measured in kilograms of CO_2 per kWh output, where in this case it will be based upon the GWP of shore electricity.

In summary, the primary aims of this paper are to assess the potential of flow-batteries in coastal ferry applications. This will be achieved by means of an electrical equivalent circuit model coupled with a temperature prediction model, developed in Section 2, to assess whether the temperature limits are exceeded for a particular use case. Section 3 will then discuss the results, including a breakdown of cost and emissions per voyage compared to other power systems.

2. Redox flow-battery model development

Here the development of the electrical and thermal model will be discussed, along with the process involved for sizing the system, where Table 2 presents the parameters used.

Table 2
Electro-thermal model parameters.

Parameter	Value
Specific heat of the electrolyte, C_p	3200 J kg^{-1} K^{-1} [28]
Electrolyte density, ρ	1354 kg m^{-3} [28]
Electrolyte specific energy, e	20 Wh kg^{-1}
Electrolyte viscosity, μ	0.006 kg m^{-1} s^{-1} [24]
Electrolyte conductivity, σ	20 Ω^{-1} m^{-1} [24]
Thickness of polypropylene tank wall, θ	0.025 m
Thermal conductivity of polypropylene, k	0.16 W m^{-1} K^{-1} [28]
Convection heat transfer coeff.: tank inner top/bottom wall, h_{11}	270.1 W m^{-2} K^{-1} [28]
Convection heat transfer coeff.: tank inner cylinder wall, h_{12}	405.2 W m^{-2} K^{-1} [28]
Convection heat transfer coeff.: tank outer top/bottom wall, h_{21}	3.5 W m^{-2} K^{-1} [28]
Convection heat transfer coeff.: tank outer cylinder wall, h_{22}	5.3 W m^{-2} K^{-1} [28]
Electrons transferred, z	1
Faraday's constant, F	96,485C mol^{-1}
Concentration of vanadium, c	1600 mol m^{-3} [28]
Gas constant, R	8.314C mol^{-1} K^{-1}
Number of cells per stack in the ferry, n_{stack}	600
Number of stacks in the ferry, n_{string}	20
Electrode area per cell, A_{cell}	0.078 m^2 [24]
Electrode thickness, D_{cell}	0.003 m [24]
Electrode length, L_{cell}	0.26 m [24]
Electrode width, W_{cell}	0.3 m [24]
Electrode permeability, k_{perm}	1.685 $\times 10^{-10}$ m^2 [24]

2.1. Redox flow-battery sizing

Sizing of the battery will depend mainly on the maximum load of the use-case, whereas the electrolyte volume is scaled up to suit the energy storage requirements. In transport applications the energy stored will be limited by the mass or volume available.

The number of cells per stack, n_{stack}, is increased until an adequate stack OCV is attained, which is based upon the motor requirements. Next, the number of stacks, n_{string}, is increased until the max load requirement is met. The current density per cell should be taken into consideration also, where it should be as close as possible to the current density used to obtain the ECM data. This model uses the ECM data and electrode size from the work of Zhao et al. [24], detailed further in Section 2.2. Once the stack and string numbers are defined, the total volume of electrolyte inside the battery can be found by,

$$V_{batt} = V_{hc} \times 2 \times n_{stack} \times n_{string} \tag{3}$$

where the half-cell volume, V_{hc}, is found by,

$$V_{hc} = A_{cell} \times D_{cell} \times \varepsilon \tag{4}$$

where the electrode porosity, Ɛ, is assumed to be 0.9 [31].

Finally, assuming the use of a light-weight design, the mass of the battery unit is then approximated by,

$$M_{batt} = V_{batt} \times \rho \times 4 \tag{5}$$

The load profile for a coastal ferry operating in Danish waters is used [8], discussed in detail later, where the diesel systems mass and volume are known to be 156,000 kg and 294 m^3 respectively. The VRFB system mass limit, M_{limit}, or system volume limit, V_{limit} will be limited to that of the diesel system. The remaining mass of electrolyte available for the tanks is then found after deducting the mass of the battery unit from M_{limit},

$$M_r = M_{limit} - M_{batt} \tag{6}$$

where each tank will store,

$$M_{tank} = \frac{M_r}{2} \tag{7}$$

and thus,

$$V_{tank} = \frac{M_{tank}}{\rho_{el}} \tag{8}$$

The total positive or negative electrolyte is then found by,

$$V_+ \; or \; V_- = V_{tank} + \frac{V_{batt}}{2} \tag{9}$$

Finally, the stored energy in Watt-hours is found by,

$$System\ Energy = (V_+ + V_-) \times \rho \times e \tag{10}$$

In this scenario the volume limit was not reached.

2.2. Electrical equivalent circuit modelling

The equivalent circuit model was developed using a MATLAB Simulink Simscape environment. A typical ECM is shown in Fig. 2, where the open-circuit voltage is a function of the battery state of charge. The total resistance is modelled by R_0 and R_1, and the dynamic response is modelled by the parallel resistor-capacitor pair, R_1 and C_1. The resistive and capacitive values can be obtained by performing a series of charge and discharge pulse tests such as the hybrid pulse power characterization (HPPC) method [32], or using electrochemical impedance spectroscopy (EIS) [33,34]. Flow battery EIS tests can suffer from low frequency disturbances due to the pulsing nature of the peristaltic pumps, where a gravity siphon can eliminate this issue [35].

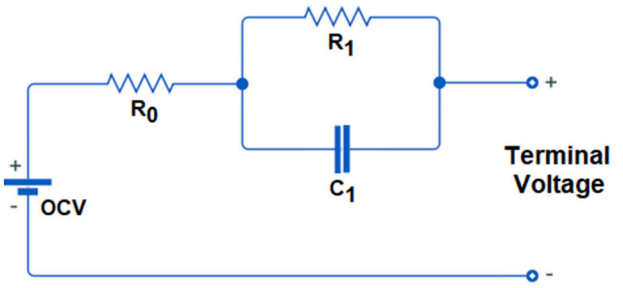

Fig. 2. First-order electrical equivalent circuit model.

The present model utilizes ECM parameters from a 15 cell stack by Zhao et al. [24], treating it as a 15 cell battery module in the overall battery unit. The battery was configured so that the current density at full load was kept in the region of 160 mA/cm^2, as the ECM values used were obtained at this current density. This was necessary in order to get a representative battery model, since the behavior of a flow-battery does not scale linearly with increased electrode size [36]. In an ideal case this model would use dynamic response data from a megawatt scale battery, though there is limited data available on this scale.

The open circuit voltage for the 15-cell module is modelled using the following simplified equation [24],

$$V_{OCV_{module}} = 15 \times \left(E_0 + \frac{2RT}{F} ln \frac{SoC}{1 - SoC} \right) \tag{11}$$

where E_0 is the standard electrode potential, and is set to 1.39 V. The temperature is set to 25 °C, where the ECM model does not consider changes in temperature. The equivalent circuit model determines the terminal voltage for the 15-cell module by,

$$V_{15CellModule} = V_{ocv_{module}} + IR_{0_{module}} + V_{RC1_{module}} \tag{12}$$

where the resistive and capacitive components for the 15-cell stack, R_0, R_1 and C_1 are 0.0104 Ω, 0.0097 Ω and 1110 F respectively, obtained using a current density and flow rate of 160 mA/cm^2 and 4 L/min [24]. Many studies demonstrate far higher current densities [37,38], however the objective is to ensure minimal degradation using a modest current density, so that the 20 year lifespan can be utilized to bring down the cost per year of ownership. The 15-cell module voltage is then scaled up by adding the modules in a string to meet the system voltage requirements. Forty modules were required to reach the desired 600 cell string in order to output an appropriate voltage for the motor. The current density is then reduced by adding more strings, until the target current density of 160 mA/cm^2 is attained for steady state cruising. The state of charge is then modelled by,

$$SoC_t = SoC_{t-1} + \left(\frac{System\ Current}{System\ Capacity \times 3600} \right) \delta t \tag{13}$$

where the system capacity has the units Amp-hours, found by dividing the Watt-hour capacity by the system nominal voltage.

Flow batteries using a stacked arrangement inevitably suffer a parasitic loss referred to as shunt currents. These losses arise as a result of using common electrolyte manifolds [39]. It's possible to model shunt currents using equivalent circuit methods, where resistors are used to represent the ionic resistance of the pipe networks [40]. Fig. 3 shows the layout of one half-system, where it can be seen that each string has piping that connects directly to the tank using long pipes to minimize shunt currents. This is done at the cost of increased pumping losses in the pipes, which are generally small due to the use of plastic piping and low flow rates, as will be seen in Section 3.

Looking at Fig. 4, the shunt current model by Zhao et al. [24] has been extended to incorporate the additional piping networks used in the present work. It should be noted that industrial systems would typically use significantly larger electrodes with a lesser number of strings to reduce shunt currents, however the 15-cell kilowatt scale stack has been experimentally validated [41] and thus will be utilized in the present work. The resistor values used in the shunt current model can be found in Table 3, found using the following equation,

$$R = \frac{L}{\sigma A} \tag{14}$$

where 'L' and 'A' are the length and cross-sectional area of the pipe section, and 'σ' is the electrolyte conductivity.

In order to reduce the complexity of the ferry model, the shunt current model was run separately at 50 % SoC at 160 mA/cm^2. The average shunt current is then multiplied by the nominal string voltage and the number of strings, then applied as a constant on the demanded load.

2.3. Hydraulic circuit model

In order to consider the net energy efficiency of the system it is necessary to incorporate the power losses associated with pumping the electrolyte through the system. Firstly, the hydraulic resistance per cell is found using Darcy's equation,

$$\widetilde{R}_{cell} = \frac{\mu \times L_{cell}}{k_{perm} \times W_{cell} \times D_{cell}} \tag{15}$$

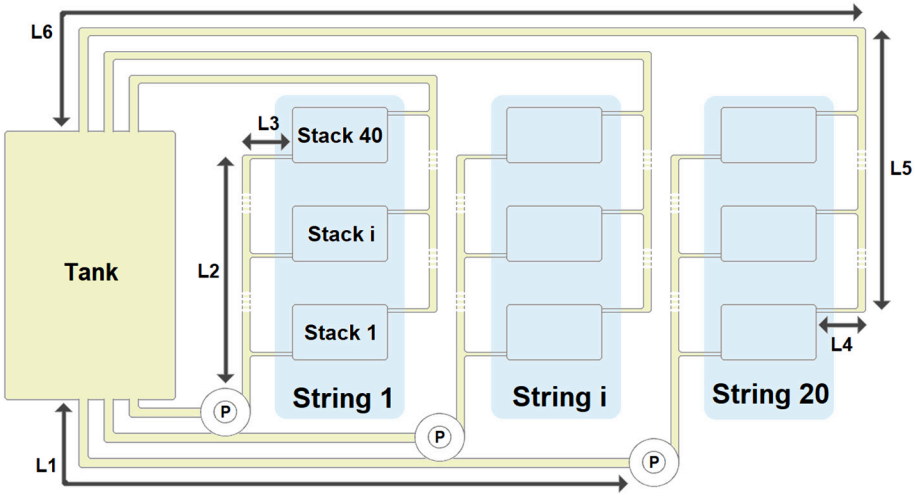

Fig. 3. System layout.

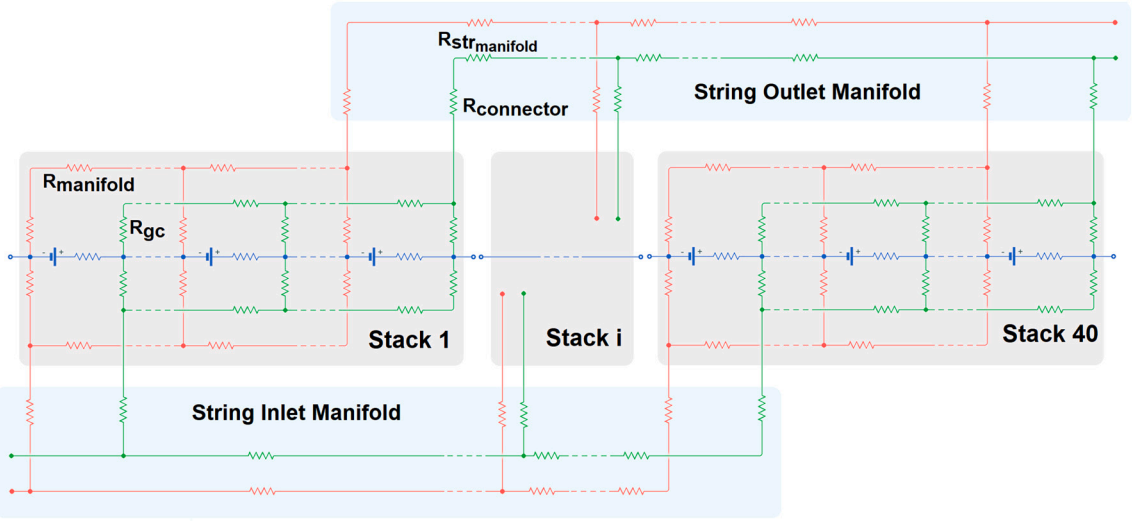

Fig. 4. Shunt current equivalent circuit model for a single string, where the blue components represent the cells and their internal resistance, while the red and green circuits represent the ionic resistances of the guide channel and manifold networks in the anolyte and catholyte sides of the system respectively. (For interpretation of the references to colour in this figure legend, the reader is referred to the web version of this article.)

Table 3
Shunt current model resistance values.

Parameter	Resistance (Ω)
Stack guide channel resistance, R_{gc}	5333.33 [24]
Stack manifold resistance, $R_{manifold}$	1.25 [24]
Stack manifold to string manifold connector resistance, $R_{connector}$	127.32
Manifold section between each stack resistance, $R_{str_{manifold}}$	9.05

Next, the pressure drop across a single stack is determined by,

$$\Delta p_{stack} = \frac{Q \times \widetilde{R}_{cell}}{15} \tag{16}$$

The flow rate of each stack was maintained at a constant of 4 L/min, in line with the ECM data used by Zhao et al. [24], and thus the system flow rate is scaled up according to the number of stacks used.

The minor losses and frictional losses in the external piping network are also considered. Looking at the frictional losses first, the Reynolds number is found by,

$$Re = \frac{\rho V D}{\mu} \tag{17}$$

where 'V' is the velocity of the electrolyte, and 'D' is the internal diameter of the pipe. The pipe lengths and diameters labelled in Fig. 3 are listed in Table 4.

The friction factor for a pipe section is then found by,

$$f = \frac{64}{Re}\ (For\ Re < 2000), f = 0.316 Re^{-0.25}\ (For\ 4000 < Re < 10000) \tag{18}$$

The frictional losses can then be found using the Darcy-Weisbach equation,

$$h_f = f \frac{L}{D} \frac{V^2}{2g} \tag{19}$$

where 'L' is the length of the pipe section. Next, the minor losses are found using the following,

$$h_m = K_L \frac{V^2}{2g} \tag{20}$$

where 'K_L' are the minor loss coefficients, found in Table 5. The pressure drop across the pipe network can then be found using the Bernoulli equation, where the first three terms in brackets can be assumed zero for model simplicity,

$$\Delta p_{piping} = \rho g \left(h_{work} - \frac{V^2}{2g} - \Delta z - h_f - h_m \right) \tag{21}$$

Finally, the pump load is found by,

$$\Delta P_{pump} = \frac{\left(\Delta p_{stacks} + \Delta p_{piping}\right) \times \left(Q_+ + Q_-\right)}{\eta_{pump}} \tag{22}$$

where the pump efficiency, η_{pump}, is set to 0.5 [41]. This pump load is added to the demanded load.

2.4. Thermal modelling

The temperature prediction of the electrolyte is based upon the conservation of energy. A number of assumptions are made without losing generality [28],

Heat is only generated via the resistance of the cells;

1. Heat transfer between the cells and the surroundings only occurs between the surrounding air and the electrolyte tanks;

Table 4
Pipe lengths and diameters.

Pipe section	Length (m)	Diameter (m)
L1	25	0.075
L2	25	0.075
L3	0.2	0.0254
L4	0.2	0.0254
L5	25	0.075
L6	25	0.075

Table 5
Minor loss coefficients.

Component	Loss coefficient K_L
Tank into pipe	0.4
Flanged 90° bend	0.2
Reduction in pipe	0.33
Expansion in pipe	0.56
Pipe into tank	1

2. Electrolyte volumes in the tanks and cells are constant during battery operation;
3. Electrolyte is perfectly mixed at all times;
4. The electrolyte tank outer surfaces are under free-convection conditions in the engine room
5. The electrolyte tank inner surfaces are considered to be free-convection due to the flow-rate being relatively small when compared to the tank volume

The resulting energy balance equations are shown in Eqs. (23), (24) and (25) for the battery system, positive electrolyte tank and negative electrolyte tank respectively.

$$C_p\rho V_{batt}\frac{dT_{batt}}{dt} = Q_+C_p\rho(T_+ - T_{batt}) + Q_-C_p\rho(T_- - T_{batt}) + I^2_{stack}R_{stack}n_{string} \tag{23}$$

$$C_p\rho V_+\frac{dT_+}{dt} = Q_+C_p\rho(T_{batt} - T_+) + UA(T_{air} - T_+) \tag{24}$$

$$C_p\rho V_-\frac{dT_-}{dt} = Q_-C_p\rho(T_{batt} - T_-) + UA(T_{air} - T_-) \tag{25}$$

While the ferry is using the direct swapping method for the electrolyte at the port, Eqs. (24) and (25) become,

$$C_p\rho V_+\frac{dT_+}{dt} = Q_+C_p\rho(T_{batt} - T_+) + Q_{port}C_p\rho\left(T_{port} - T_+\right) + UA(T_{air} - T_+) \tag{26}$$

$$C_p\rho V_-\frac{dT_-}{dt} = Q_-C_p\rho(T_{batt} - T_-) + Q_{port}C_p\rho\left(T_{port} - T_-\right) + UA(T_{air} - T_-) \tag{27}$$

where Q_{port} and T_{port} are the flow rate of the electrolyte exchange and the temperature of the electrolyte at the port respectively. Air temperature is held constant at 298 K, and while ported it is assumed that the flow battery on-board the ferry continues to circulate electrolyte within its own system to flush out depleted electrolyte and reduce the temperature of the electrolyte in the battery unit. This is important as temperature management during stand-by conditions is critical to avoid solute precipitation [42]. Each of the ports which the ferry docks at has the same electro-thermal model in place, though the electrolyte volume at each of the ports is twice that of the ferry. The flow rate for electrolyte swapping of each half of the system is found by,

$$Q_{port} = \frac{V_+ \text{ or } V_-}{t_{port}} \tag{28}$$

where t_{port} is the time spent in the port.

In order to define the overall heat transfer coefficient for each tank it is first necessary to define the tank dimensions. For simplicity it is assumed that the tank will be cylindrical, and have a 1:1 height to width ratio.

The electrolyte tanks are assumed to be polypropylene, where the heat transfer coefficient for the cylindrical wall of the tank, U_{cyl}, and the top or bottom surface of the tank, U_{flat}, are found by,

$$U_{cyl} = \frac{1}{\left({}^1/_{h_{11}}\right) + \left({}^{r_{tank}}/_{k}\right)ln\left({}^{r_{tank}+\theta}/_{r_{tank}}\right) + \left({}^{r_{tank}}/_{r_{tank}+\theta}\right)\left({}^1/_{h_{21}}\right)} \tag{29}$$

$$U_{flat} = \frac{1}{{}^1/_{h_{12}} + {}^{\theta}/_{k} + {}^1/_{h_{22}}} \tag{30}$$

where h_{11} and h_{21} are the inner and outer heat transfer coefficient of the top/bottom surfaces respectively, while h_{12} and h_{22} are the inner and outer heat transfer coefficient of the cylindrical surface respectively [28].

The overall heat transfer coefficient can then be identified as,

$$UA = U_{cyl}A_{cyl} + 2U_{flat}A_{flat} \tag{31}$$

where the areas of the two surfaces are,

$$A_{cyl} = 2\pi \times r_{tank} \times h_{tank} \tag{32}$$

$$A_{flat} = \pi \times r^2_{tank} \tag{33}$$

3. Results and discussion

The resulting system sizing achieved following the methodology in Section 2 can be seen in Table 6. The system has the same mass as the original diesel system, at 156 t, and is therefore mass constrained. The VRFB system volume was approximately 115 m^3, where the original diesel system was 294 m^3 including a 140 m^3 fuel tank.

3.1. Single trip and swapping method

The ferry embarks on sixteen 1-hour trips per day, where the first trip can be seen in Fig. 5. This is an averaged load profile for the original diesel system, where the only difference is that the diesel system continues to power the ancillaries when ported. As the ferry disembarks there is a ramp up in demanded load before entering steady-state cruising mode. The battery voltage gradually drops in this mode as the state of charge is decreasing, resulting in a slight increase in the magnitude of cell current density to meet the demanded load. The load then begins to ramp down and the ferry is stationary in the port at 2785 s until 3600 s.

While ported, the ferry ancillaries are powered by the grid and the port is exchanging electrolyte from the port VRFB to the ferry VRFB, resulting in a rise in the state of charge and battery voltage. The port batteries have the same stack size as the ferry, with twice the capacity of the ferry.

It can be seen that after a single trip the temperatures of the ferry stack and tanks have remained within the safe operating limits. The stack temperature begins to drop initially as the load is reduced, and then both the stack and tank temperatures drop as electrolyte is exchanged with the port.

The state of charge of the system drops to 58 % after the voyage, indicating at first that a VRFB ferry is viable from an energy capacity point of view. This method of electrolyte swapping shall be called direct swapping. Looking at a full day of operation in Fig. 6, direct swapping eventually reaches a stabilization window of operation, where each trip starts at 66 % and is reduced to 20 %. This results from the port and the ferry mixing electrolytes, approaching a final SoC somewhere between the port and ferry initial SoC.

This paper proposes a new method for electrolyte swapping, whereby the ferry and ports would have two additional electrolyte tanks, termed pre-chambers, as seen in Fig. 7 denoted by 'PC'. When the ferry needs to swap electrolyte, the port will pump fully charged electrolyte into the ferry pre-chambers, while the ferry pumps its depleted electrolyte into the port pre-chambers. Once the port has filled the ferry pre-chamber with charged electrolyte, and the ferry has filled the port pre-chamber with depleted electrolyte, the pre-chambers then release the electrolyte into the empty tanks. This enables the ferry to receive the

Table 6
RFB ferry system sizing.

Parameter	Value
Dry battery unit mass	22,813 kg
Battery unit electrolyte mass	7604 kg
Tank electrolyte mass	125,584 kg
System mass	156,000 kg
System capacity	2.89 MWh
System specific energy	18.52 Wh kg^{-1}

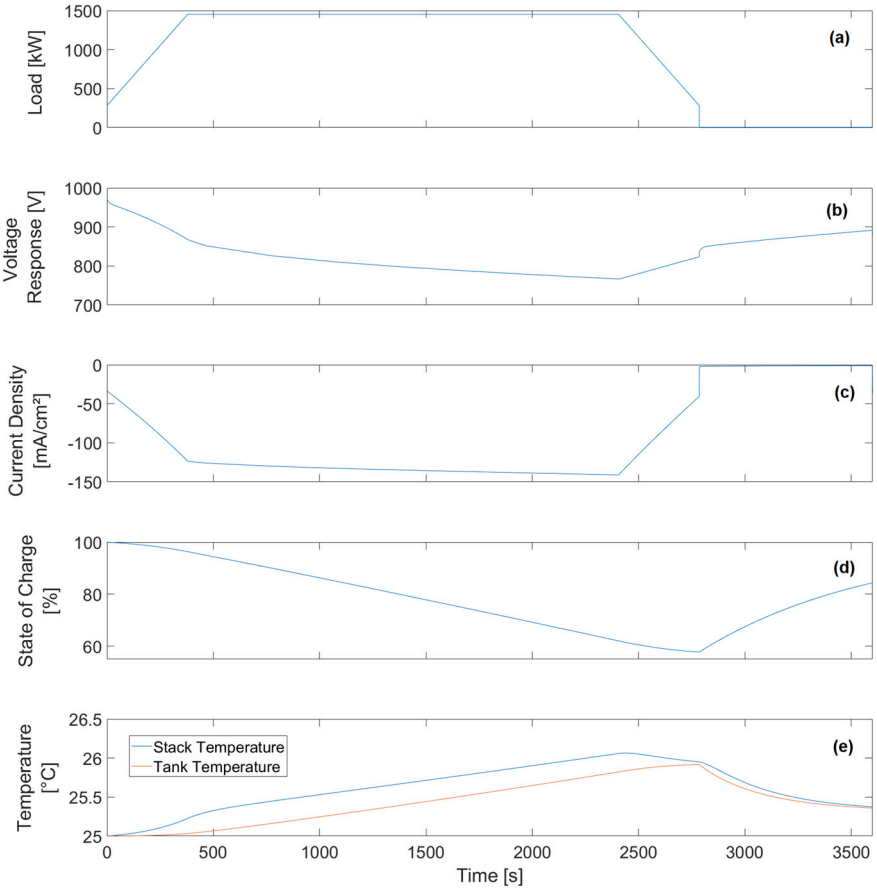

Fig. 5. A single trip between ports showing the (a) ferry battery load demanded; (b) ferry battery voltage response; (c) ferry battery current density per cell; (d) ferry battery state of charge; (e) ferry electrolyte temperature in the battery and tanks.

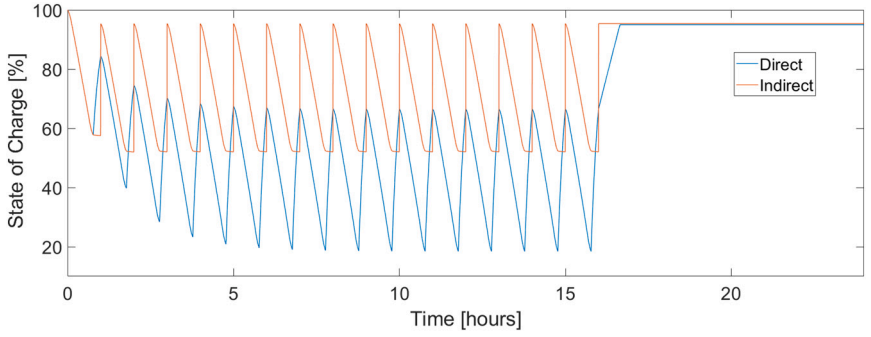

Fig. 6. Comparison of state of charge operating windows for direct and in-direct electrolyte swapping.

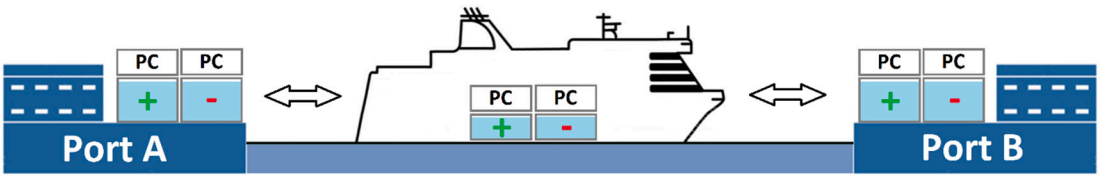

Fig. 7. RFB E-Ferry operating between two ports.

electrolyte without the swapping process reducing the capacity. After considering the volume of the main tanks and battery unit, there was still sufficient room to accommodate the pre-chambers on the ferry.

Fig. 6 shows how employing indirect swapping results in a significant difference in the state of charge stable operating window, where each voyage now starts at 95 % (to prevent gassing) and ends at 52 %. This finding is of great importance, as the increased state of charge means that the efficiency of the system is improved and the range is increased.

Higher state of charge means a higher operating voltage, which results in a lower current density. The operating temperature of the system is then also reduced as a result, due to the I^2R Ohmic heating relationship. Any future development of redox flow-batteries in transport applications should strongly consider using indirect swapping if electrolyte swapping is employed. If the vehicle is limited for space, pre-chambers in just the port/station are sufficient, though this will result in a slower swapping process.

The output for the string shunt current is shown in Fig. 8. It is evident that shunt current plays a very serious role in systems with a large stack size. At 50 % SoC the average string shunt current is 16.57 A, 13 % of the applied load, equating to a power loss of 278.39 kW. This could be reduced by utilizing a more complex piping network at the cost of additional pumping losses, or by using industrial scale cells which are large enough to justify using a single pump and tank for a portion of the string. The pumping losses associated with the piping network and the stacks was calculated to be <1 % of the demanded load.

3.2. Long term usage and cooling requirements

When looking at the temperature of a single trip in Fig. 5 (a) or a day of operation, the ferry and ports require no cooling, as the temperatures stay well within the safe operating limits. The simulation was then extended over a number of months until the temperature reached a stable operating window. Fig. 9 shows the peak temperature of each day of operation over a fifteen week period using indirect swapping.

By introducing a cooling system in each of the port electrolyte tanks it is possible to bring the ferry temperatures down significantly, where the cooling power was iteratively increased until the temperature stabilized just below 40 °C. This required 62 kW of cooling per port tank, without needing to add additional mass or volume to the ferry. It should be noted that the atmospheric temperature was held constant at 25 °C which is a worst case scenario for Danish waters, where typically the temperatures would be far lower. In reality less cooling power would be required at the ports, and could be optimized based on the actual conditions and weather forecasts.

3.3. Cost and emissions

This section will discuss the costs and emissions in comparison to original diesel system and the fuel-cell hybrid system developed by Wu et al. [8]. Wu used the Danish commercial grid energy costs and GWP of 0.09 $ / kWh and 0.17 kg CO_2 / kWh respectively, which shall also be used for the flow-battery scenario.

Looking at Table 7, system B represents the findings from Wu et al.

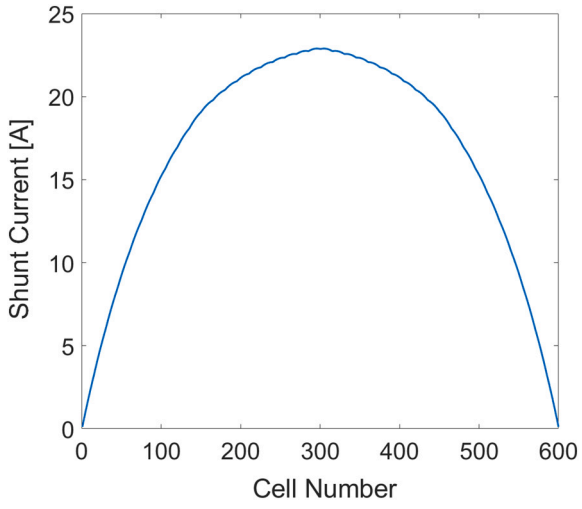

Fig. 8. Shunt current distribution along a string of 40 stacks.

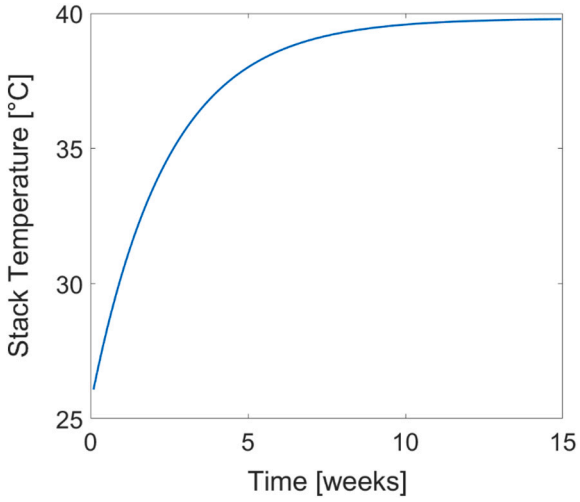

Fig. 9. Daily peak stack temperatures over fifteen weeks of operation with 62 kW of cooling in each tank at the ports.

Table 7
Cost and emissions breakdown between the various systems.

		Cost [$]	GWP emissions [kg CO_2]
System A	Diesel engine	46	–
Diesel [8]	Diesel fuel	168	838
	Shore electricity	4	4
	Total	**218**	**842**
System B	Fuel cell	238	–
Fuel cell – Li ion	Hydrogen	368	67
Hybrid [8]	Battery	65	–
	Shore electricity	39	123
	Total	**710**	**190**
System C	Flow battery	77	–
Flow battery	Electrolyte	28	–
(Indirect swapping)	Shore Electricity	172	326
	Total	**277**	**326**

[8]. The costs associated with the fuel cell and battery represent the degradation over the lifespan of the components. It can be seen that the fuel cell degradation and the hydrogen costs result in an overall cost per voyage being more than three times greater than the initial diesel system. However, the fuel cell hybrid does offer a marked reduction in GWP versus system A. Furthermore, as the technology matures, it is likely that the large expense associated with the proton exchange membranes will drop, in addition to the costs and GWP associated with manufacturing the hydrogen fuel [43].

System C presents the findings of this work, also displayed in Fig. 10.

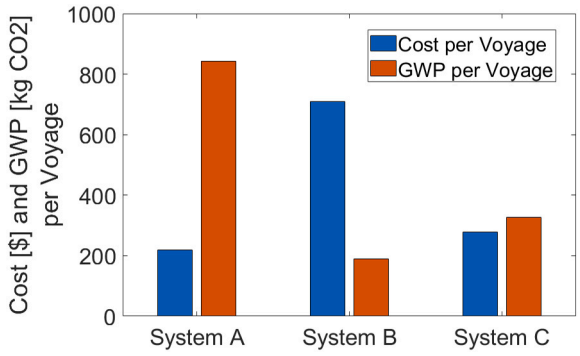

Fig. 10. Cost and emissions comparison between the various systems, where system A, B and C represent the Diesel, Fuel-cell/Li-ion, and Flow-battery systems respectively.

It can be seen that the flow battery system possesses a cost per voyage that can compete with the original diesel system, while offering a threefold reduction in GWP. Additionally, the flow-battery system can be improved further by utilizing green energy sources to recharge the port batteries, such as tidal, wind and solar energy. It should also be noted that the electrolyte can be reused after the battery is replaced, where the electrolyte accounts for 27 % of the capital cost in this application.

4. Conclusion

An electro-thermal RFB model has been developed which considers a RFB ferry voyaging between two ports, each of which have RFBs to provide electrolyte swapping for the ferry. It has been found that vanadium redox flow-batteries show real potential in coastal ferry applications. Electrolyte swapping is the key enabler in making this technology viable, where indirect swapping utilizing pre-chambers was found to be optimal over direct swapping as it enables the ferry to operate at a higher state of charge. A cooling system in just the port battery systems is sufficient to keep the ferry electrolyte temperatures under control and within the safe operating limits. The cost per voyage was shown to be close to that of the mainstream diesel system and significantly less than the fuel-cell hybrid, owing to the long lifespan of the flow-battery. The GWP of the flow-battery is more than three times less than the diesel system, and has potential to drop much further with green energy powering the port batteries. Flow battery costs and GWP is expected to improve further versus the diesel engine, as flow batteries are in a state of rapid development. Future work could consider cabin temperature management and other marine applications, where the system can be scaled for most applications with a voyage duration of around 1 h.

Funding

This work was supported by an EPSRC studentship (EP/N509541/1) with an industrial top-up by HORIBA MIRA.

CRediT authorship contribution statement

Richard Woodfield: Conceptualization, Methodology, Software, Investigation, Writing – Original Draft, Writing – Review & Editing.
Stephen Glover: Writing – Review & Editing, Supervision.
Robert Watson: Writing – Review & Editing, Supervision.
Peter Nockemann: Writing – Review & Editing, Supervision.
Richard Stocker: Writing – Review & Editing, Supervision.

Declaration of competing interest

The authors declare that they have no known competing financial interests or personal relationships that could have appeared to influence the work reported in this paper.

Data availability

Data will be made available on request.

References

[1] O.B. Inal, C. Deniz, Assessment of fuel cell types for ships: based on multi-criteria decision analysis, J. Clean. Prod. 265 (2020), 121734.
[2] P. Ni, X. Wang, H. Li, A review on regulations, current status, effects and reduction strategies of emissions for marine diesel engines, Fuel 279 (June) (2020).
[3] S. Bengtsson, E. Fridell, K. Andersson, Environmental assessment of two pathways towards the use of biofuels in shipping, Energy Policy 44 (2012) 451–463.
[4] R. Tan, O. Duru, P. Thepsithar, Assessment of relative fuel cost for dual fuel marine engines along major Asian container shipping routes, Transp. Res. Part E Logist. Transp. Rev. 140 (April) (2020), 102004.
[5] H. Thomson, J.J. Corbett, J.J. Winebrake, Natural gas as a marine fuel, Energy Policy 87 (2015) 153–167.
[6] E. Gagatsi, T. Estrup, A. Halatsis, Exploring the potentials of electrical waterborne transport in Europe: the E-ferry concept, Transp. Res. Procedia 14 (2016) 1571–1580.
[7] B.V. Sasank, N. Rajalakshmi, K.S. Dhathathreyan, Performance analysis of polymer electrolyte membrane (PEM) fuel cell stack operated under marine environmental conditions, J. Mar. Sci. Technol. 21 (3) (2016) 471–478.
[8] P. Wu, R. Bucknall, Hybrid fuel cell and battery propulsion system modelling and multi-objective optimisation for a coastal ferry, Int. J. Hydrog. Energy 45 (4) (2020) 3193–3208.
[9] C.H. Choi, et al., Development and demonstration of PEM fuel-cell-battery hybrid system for propulsion of tourist boat, Int. J. Hydrog. Energy 41 (5) (2016) 3591–3599.
[10] P. Alotto, M. Guarnieri, F. Moro, Redox flow batteries for the storage of renewable energy: a review, Renew. Sust. Energ. Rev. 29 (2014) 325–335.
[11] M. Uhrig, S. Koenig, M.R. Suriyah, T. Leibfried, Lithium-based vs. vanadium redox flow batteries - a comparison for home storage systems, Energy Procedia 99 (March) (2016) 35–43.
[12] J.R. Gouveia, E. Silva, T.M. Mata, A. Mendes, N.S. Caetano, A.A. Martins, Life cycle assessment of a renewable energy generation system with a vanadium redox flow battery in a NZEB household, Energy Rep. 6 (2020) 87–94.
[13] T. Kaizuka, T. Sasaki, Evaluation of control maintaining electric power quality by use of rechargeable battery system, Response 1 (WINTER MEETING) (2001) 88–93.
[14] T. Shibata, T. Kumamoto, Y. Nagaoka, K. Kawase, K. Yano, Redox flow batteries for the stable supply of renewable energy, SEI Tech. Rev. 76 (2013) 14–22.
[15] A.Z. Weber, M.M. Mench, J.P. Meyers, P.N. Ross, J.T. Gostick, Q. Liu, Redox flow batteries: a review, J. Appl. Electrochem. 41 (10) (2011) 1137–1164.
[16] M.R. Mohamed, S.M. Sharkh, F.C. Walsh, Redox flow batteries for hybrid electric vehicles: progress and challenges, in: " 5th IEEE Veh. Power Propuls. Conf. VPPC '09, 2009, pp. 551–557.
[17] Y. Li, X. Zhang, J. Bao, M. Skyllas-Kazacos, Studies on optimal charging conditions for vanadium redox flow batteries, J. Energy Storage 11 (2017) 191–199.
[18] J. Campillo, N. Ghaviha, N. Zimmerman, E. Dahlquist, Flow batteries use potential in heavy vehicles, in: Electr. Syst. Aircraft, Railw. Sh. Propulsion, ESARS vol. 2015-May, 2015, pp. 1–6.
[19] L. Barelli, G. Bidini, P.A. Ottaviano, D. Pelosi, Vanadium redox flow batteries application to electric buses propulsion: performance analysis of hybrid energy storage system, J. Energy Storage 24 (May) (2019), 100770.
[20] MSE International, FLO-MAR project validates flow batteries to help decarbonisation of vessels and improve air quality in ports [Online]. Available: https://www.mseinternational.org/projects/?story_id=175, 2021 [Accessed: 16-May-2022].
[21] MSE International, BlueStor Port-based novel energy storage project overview [Online]. Available: https://www.mseinternational.org/projects/?story_id=429, 2022 [Accessed: 16-May-2022].
[22] Equasis, The world murchant fleet in 2019 [Online]. Available: https://www.equasis.org/EquasisWeb/public/PublicStatistic?fs=HomePage, 2019 [Accessed: 01-Jan-2021].
[23] Q. Xu, T.S. Zhao, Fundamental models for flow batteries, Prog. Energy Combust. Sci. 49 (2015) 40–58.
[24] Y. Zhang, J. Zhao, P. Wang, M. Skyllas-Kazacos, B. Xiong, R. Badrinarayanan, A comprehensive equivalent circuit model of all-vanadium redox flow battery for power system analysis, J. Power Sources 290 (2015) 14–24.
[25] M.R. Mohamed, H. Ahmad, M.N.A. Seman, S. Razali, M.S. Najib, Electrical circuit model of a vanadium redox flow battery using extended Kalman filter, J. Power Sources 239 (2013) 284–293.
[26] A. Bhattacharjee, A. Roy, N. Banerjee, S. Patra, H. Saha, Precision dynamic equivalent circuit model of a Vanadium Redox Flow Battery and determination of circuit parameters for its optimal performance in renewable energy applications, J. Power Sources 396 (November 2017) (2018) 506–518.
[27] A. Bhattacharjee, H. Saha, Development of an efficient thermal management system for vanadium redox flow battery under different charge-discharge conditions, Appl. Energy 230 (September) (2018) 1182–1192.
[28] A. Tang, S. Ting, J. Bao, M. Skyllas-Kazacos, Thermal modelling and simulation of the all-vanadium redox flow battery, J. Power Sources 203 (2012) 165–176.
[29] A. Trovò, A. Saccardo, M. Giomo, M. Guarnieri, Thermal modeling of industrial-scale vanadium redox flow batteries in high-current operations, J. Power Sources 424 (April) (2019) 204–214.
[30] T. Lütha, S. König, M. Suriyah, T. Leibfried, Passive components limit the cost reduction of conventionally designed vanadium redox flow batteries, Energy Procedia 155 (2018) 379–389.
[31] C.L. Hsieh, P.H. Tsai, N.Y. Hsu, Y.S. Chen, Effect of compression ratio of graphite felts on the performance of an all-vanadium redox flow battery, Energies 12 (2) (2019) 1–12.
[32] Z. Wei, S. Meng, K.J. Tseng, T.M. Lim, B.H. Soong, M. Skyllas-Kazacos, An adaptive model for vanadium redox flow battery and its application for online peak power estimation, J. Power Sources 344 (2017) 195–207.
[33] M. Messaggi, C. Rabissi, C. Gambaro, L. Meda, A. Casalegno, M. Zago, Investigation of vanadium redox flow batteries performance through locally-resolved polarisation curves and impedance spectroscopy: insight into the effects of electrolyte, flow field geometry and electrode thickness, J. Power Sources 449 (August2020) (2019) 227588.
[34] A. Barai, et al., A comparison of methodologies for the non-invasive characterisation of commercial Li-ion cells, Prog. Energy Combust. Sci. 72 (2019) 1–31.

[35] C.-N. Sun, F.M. Delnick, D.S. Aaron, A.B. Papandrew, M.M. Mench, T. A. Zawodzinski, Resolving losses at the negative electrode in all-vanadium redox flow batteries using electrochemical impedance spectroscopy, J. Electrochem. Soc. 161 (6) (2014) A981–A988.
[36] R.M. Darling, M.L. Perry, The influence of electrode and channel configurations on flow battery performance, J. Electrochem. Soc. 161 (9) (2014) A1381–A1387.
[37] M. Guarnieri, A. Trovò, G. Marini, A. Sutto, P. Alotto, High current polarization tests on a 9 kW vanadium redox flow battery, J. Power Sources 431 (May) (2019) 239–249.
[38] D. Reed, et al., Stack developments in a kW class all vanadium mixed acid redox flow battery at the pacific northwest national laboratory, J. Electrochem. Soc. 163 (1) (2016) A5211–A5219.
[39] M. Skyllas-Kazacos, J. McCann, Y. Li, J. Bao, A. Tang, The mechanism and modelling of shunt current in the vanadium redox flow battery, ChemistrySelect 1 (10) (2016) 2249–2256.
[40] F.T. Wandschneider, S. Röhm, P. Fischer, K. Pinkwart, J. Tübke, H. Nirschl, A multi-stack simulation of shunt currents in vanadium redox flow batteries, J. Power Sources 261 (2014) 64–74.
[41] S. Kim, et al., 1 kW/1 kWh advanced vanadium redox flow battery utilizing mixed acid electrolytes, J. Power Sources 237 (2013) 300–309.
[42] A. Tang, J. McCann, J. Bao, M. Skyllas-Kazacos, Investigation of the effect of shunt current on battery efficiency and stack temperature in vanadium redox flow battery, J. Power Sources 242 (2013) 349–356.
[43] M.M. Whiston, I.L. Azevedo, S. Litster, K.S. Whitefoot, C. Samaras, J.F. Whitacre, Expert assessments of the cost and expected future performance of proton exchange membrane fuel cells for vehicles, Proc. Natl. Acad. Sci. U. S. A. 116 (11) (2019) 4899–4904.